Research Article Vol. 1, No. 5 / November 2014 / Optica 350

Mid-infrared integrated waveguide modulators based on silicon-on-lithium-niobate photonics

JEFF CHILES[1] AND SASAN FATHPOUR[1,2,*]

[1]CREOL, The College of Optics and Photonics, University of Central Florida, Orlando, Florida 32816, USA

[2]Department of Electrical Engineering and Computer Science, University of Central Florida, Orlando, Florida 32816, USA

*Corresponding author: fathpour@creol.ucf.edu

Received 4 September 2014; revised 15 October 2014; accepted 15 October 2014 (Doc. ID 222548); published 18 November 2014

Heterogeneous integration techniques, such as direct bonding, have enabled solutions to many problems facing integrated photonics. In particular, the relatively new field of mid-infrared (mid-IR) integrated photonics has been hindered by the availability of functional, transparent substrates in this wavelength range. The key to achieving compact, high-performance optical modulation and frequency conversion is the monolithic integration of silicon photonics with a material with high second-order nonlinear susceptibility. By transferring large areas of thin, monocrystalline silicon to bulk lithium niobate ($LiNbO_3$) substrates, the first silicon-based platform to exploit the Pockels or linear electro-optic effect in the mid-IR range is achieved. Integrated Mach–Zehnder interferometer modulators with an extinction ratio of ~8 dB, a half-wave voltage-length product of 26 V · cm, and an on-chip insertion loss of 3.3 dB are demonstrated at a wavelength of 3.39 μm. Ultrathin optical waveguides fabricated and characterized on this platform exhibit a low transverse electric mode linear propagation loss of 2.5 dB/cm. Future capabilities such as wideband difference frequency generation for integrated mid-IR sources are envisioned for the demonstrated silicon-on-lithium-niobate platform.

OCIS codes: (130.4110) Modulators; (230.7370) Waveguides; (250.3140) Integrated optoelectronic circuits; (250.4110) Modulators; (130.3730) Lithium niobate.

http://dx.doi.org/10.1364/OPTICA.1.000350

1. INTRODUCTION

The mid-infrared (mid-IR) region of the optical spectrum (3–8 μm) is an important range for applications in remote sensing, free-space communications, and defense technology [1]. Integrated photonics offers the best outlook for achieving these functions at low cost, while maintaining good yield and consistent performance. For the targeted applications, it is desirable to use a platform that exhibits transparency at least through the first atmospheric transmission window of 3–5 μm. Although the silicon-on-insulator (SOI) platform has proven highly effective for near-infrared (near-IR) photonics [2], the presence of the buried silicon dioxide (SiO_2) layer limits its usefulness in the mid-IR range due to the onset of optical absorption [3]. Many mid-IR silicon-based platforms have been proposed and demonstrated to replace SOI, including silicon-on-sapphire [4,5], silicon-on-nitride [6], and all-silicon membrane waveguides (the all-silicon optical platform) [7].

However, the choice of a photonic platform in the mid-IR should not be restricted merely to transparency considerations. A multielement photonic circuit such as an on-chip beam combiner [8] may be composed of numerous passive and active elements, such as tunable phase shifters, optical modulators, passive routers and spectrum filters, and possibly wavelength conversion elements for accessing more efficient detectors. The materials available on the platform determine the means available to achieve these effects. Silicon photonic platforms typically enable a high integration density of passive filtering

and routing elements due to the high index contrast available in their waveguides. Additionally, third-order optical nonlinearities [9–12] are made possible by the low multiphoton absorption in the mid-IR region, but the pump power to achieve these effects is still relatively high.

Phase shifting and optical modulation has been achieved through the thermo-optic effect in silicon at speeds up to 70 kHz in the near-IR [13] and the mid-IR range at 23.8 kHz [14] on the SOI platform, but significant increases to these speeds are constrained by trade-offs with power consumption and propagation loss of the waveguides.

An alternative means to achieving on-chip phase shifts with silicon is by plasma dispersion [15], a highly CMOS-compatible approach which has been used to fabricate optical modulators in the near-IR with half-wave voltage products below 3 V · cm and data rates ranging from 10 to 50 Gbit/s [16,17]. However, higher bandwidths are achieved at the expense of extinction ratio in such devices; for instance, in Ref. [17], the bit rate of 10 Gbit/s achieves 18 dB extinction ratio, but in Ref. [16], the higher bit rate of 50 Gbit/s is accompanied by an extinction ratio of only 3.1 dB, which is not useful for long-distance communication applications. It is thus useful to consider a figure of merit for the modulation performance as the product of the maximum data rate and the extinction ratio at that rate. The modulators mentioned above exhibit products of 180 and 155 dB · Gbit/s, respectively.

Furthermore, the characteristics of plasma-dispersion-based modulators will be substantially different at longer wavelengths, as is investigated in Ref. [18]. Because of the stronger electroabsorption, a waveguide with a π phase shift induced from electrorefraction by free carriers would encounter an unavoidable absorption loss of 1.17 dB when operating at a wavelength of 4 μm. This means that pure phase modulation is unachievable with this effect in the mid-IR, limiting its usefulness for applications such as on-chip beam combining, or communication links with phase-shift-keying schemes.

Strained silicon can exhibit the Pockels effect in submicrometer waveguides in the near-IR [19], albeit with a high half-wave voltage product of 100 V · cm. With larger waveguide cross-sections in the mid-IR, inducing strain is expected to be even more difficult.

Evidently, silicon alone may not be able to simultaneously provide all the functions required for high-performance mid-IR integrated photonics. By hybridizing it with other materials, new functions can be performed. For instance, to provide enhanced modulation performance in the near-IR, silicon organic hybrid waveguides have been fabricated with low-drive voltages down to 0.52 V · mm [20].

Meanwhile, lithium niobate ($LiNbO_3$) is a mid-IR compatible material (transparent up to 5 μm wavelength) with a high electro-optic coefficient, low refractive index (~2.1), and high second-order optical nonlinearity. Thanks to the fast response of the Pockels effect, near-IR $LiNbO_3$ optical modulators have achieved speeds exceeding 100 GHz [21], though with a $V_\pi \cdot L$ of ~10 V · cm. In addition, commercially available $LiNbO_3$ modulators such as the Mach-40 005 from Covega can provide modulation speeds of 40 Gbit/s while maintaining an extinction ratio of 13 dB, giving a modulation performance product of 520 dB · Gbit/s, which is much higher than the aforementioned values in SOI-based devices. An optical modulator operating at a speed of 1.8 GHz and at a wavelength of 3.39 μm has been reported in Ti-diffused $LiNbO_3$ waveguides decades ago [22], but the low index contrast available in this platform greatly limits integration density and increases the device lengths since wide gaps are required for the electrodes.

To obtain a higher index contrast, the integration of silicon and $LiNbO_3$ has been explored for near-IR applications. One approach is top-side bonding [23,24], in which small pieces of thin $LiNbO_3$ films are bonded on top of a silicon waveguide, so that the optical mode partially overlaps the $LiNbO_3$ top cladding. However, this approach requires extra per-device processing and is only suitable for near-IR wavelengths, as it is performed on SOI substrates. Additionally, Ref. [24] utilizes a polymer bonding agent, which would induce loss in the mid-IR. Amorphous silicon has also been investigated in the near-IR based on its direct deposition on $LiNbO_3$ substrates [25,26], but the intrinsic linear loss of this material and its increasing material loss toward longer wavelengths [27] makes it unsuitable for the mid-IR spectral region.

We have recently demonstrated thin-film $LiNbO_3$ hybrid high-index contrast waveguides and modulators on oxidized silicon substrates in the near-IR [28]. The advantages over the mentioned top-side bonding approach include coupling light into $LiNbO_3$ waveguide core (rather than cladding) regions, as well as fabrication based on robust full-wafer bonding techniques rather than bonding small pieces with unreliable polymers. Unfortunately, similar to SOI, the expected loss of the oxide bottom cladding layer prohibits using our $LiNbO_3$-on-Si hybrid platform for mid-IR wavelengths.

In this work, to avoid material loss problems and to retain reliable wafer-scale processing capabilities, we have achieved the integration of crystalline silicon on $LiNbO_3$ substrates through direct wafer bonding and thin-film transfer techniques. We recently proposed and utilized this novel silicon-on-lithium-niobate (SiLN) platform (Fig. 1) to demonstrate passive waveguides at near-IR wavelengths [29]. In contrast to the discussed $LiNbO_3$-on-Si platform, SiLN employs a top silicon layer as the waveguide core material, and $LiNbO_3$ as the lower cladding. The SiLN platform has numerous practical advantages, including uninterrupted low-loss transmission

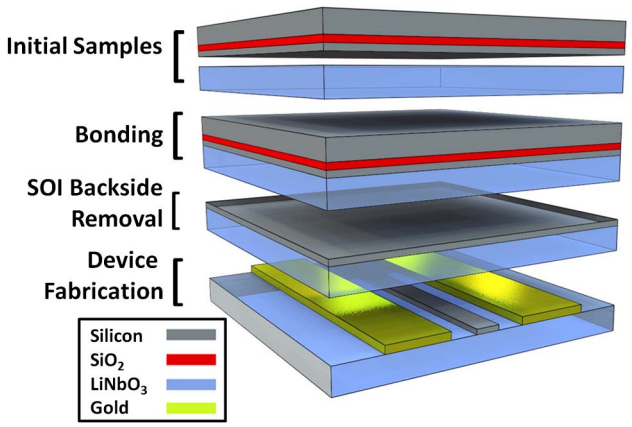

Fig. 1. Process used to prepare SiLN chips.

throughout the wavelength range of 1.2–5 μm, compatibility with silicon-processing techniques, and a strong effective second-order optical nonlinearity, which will greatly reduce the intensity threshold for achieving certain wavelength conversion functions.

In this work, mid-IR integrated waveguide modulators based on the SiLN platform are demonstrated, representing the first silicon-based photonic devices exploiting the Pockels effect in this wavelength region. First, the design and fabrication of the modulators and SiLN substrates will be described. Next, the results for passive waveguides and active devices at lower frequencies will be presented. AC modulation results at the maximum available detector speed will then be presented, followed by conclusions and remarks on the outlook of the SiLN platform.

2. METHODS

A. Design

The SiLN platform consists of a bulk X-cut $LiNbO_3$ substrate, 500 μm thick, with a 210 nm thick layer of monocrystalline silicon fusion-bonded on the top surface. This silicon layer thickness provides a large optical mode overlap with the $LiNbO_3$ substrate, while retaining sufficient mode confinement to avoid excessive bending loss at our measurement wavelength of 3.39 μm. COMSOL-based simulations of the modulator are shown in Fig. 2, with laterally spaced gold electrodes creating a horizontal electric field along the z axis underneath the fully etched silicon channel waveguide, in order to access the largest attainable electro-optic coefficient of $LiNbO_3$, $r_{33} \approx 31$ pm/V. The optical mode propagates along the y axis, with a simulated effective mode index of 2.15 for 2.1 μm wide single-mode waveguides. The gold electrodes are spaced by 8.5 μm to avoid loss induced by optical mode overlap with the metal, with an allowance for some alignment tolerance during fabrication. The optical mode overlap into the $LiNbO_3$ substrate is 56%. The simulated $V_\pi \cdot L$ is 13 V · cm for a push–pull configured modulator. The advantage of this modulator configuration is that there is no need to dope the silicon waveguide core (which would introduce optical loss), and it can in principle be operated at speeds well above 10 GHz by designing the electrodes for velocity matching as in conventional $LiNbO_3$ travelling wave modulators in the near-IR [30]. This is possible because the mechanism of modulation is the same for both SiLN and conventional $LiNbO_3$ waveguides. Additionally, due to the large optical bandwidth of MZIs, this modulator is simulated to achieve greater than 10 dB extinction ratio over an optical bandwidth of more than 500 nm with respect to center operation at 3.39 μm (Fig. 3). The bandwidth is limited by the wavelength dependence of the mode overlap into the $LiNbO_3$ substrate, which changes the $V_\pi \cdot L$ as the wavelength moves away from the center.

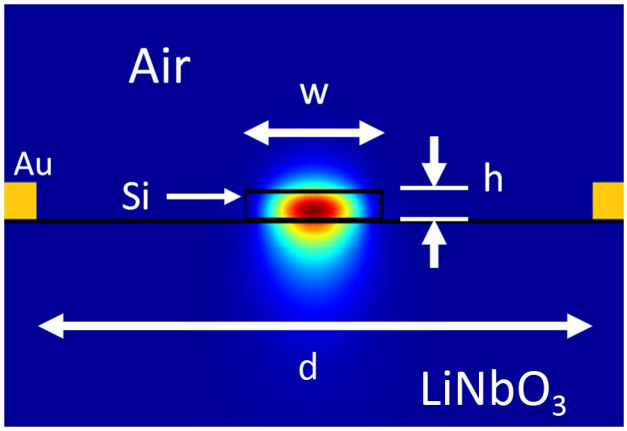

Fig. 2. Simulated mode profile (red is the peak intensity) and modulator dimensions: $w = 2.1$ μm, $h = 210$ nm, $d = 8.5$ μm. The gold rectangles represent the edges of the electrodes used for modulation.

B. SiLN Substrate Preparation

The fabrication process for preparing SiLN substrates is schematically depicted in Fig. 1. First, an SOI die and a $LiNbO_3$ die, about 1.5 cm × 1.5 cm each, were obtained. The dies were then ultrasonically cleaned in standard solvents. To activate the surfaces for direct bonding [31], they were subjected to a low-power argon plasma (with some additional oxygen in the plasma mixture to prevent out-diffusion of oxygen atoms from the $LiNbO_3$ substrates) in an inductively coupled plasma (ICP) reactive-ion etching (RIE) chamber. The dies were then heated to 100°C and bonded such that the SOI top silicon layer was in direct contact with the $LiNbO_3$ substrate, and then annealed at 170°C for 1.5 days to strengthen the bond. Then, the backside of the SOI die was removed via rapid wet-etching with a mixture of hydrofluoric acid (HF), nitric acid (HNO_3), and water. The newly exposed (formerly "buried" on the SOI) SiO_2 layer was selectively removed using buffered oxide etchant, leaving a fully intact, crystalline thin film of silicon on the top surface of the $LiNbO_3$ substrate.

C. Waveguide and Modulator Fabrication

The SiLN dies were lithographically patterned into a set of MZI modulators based on Y junction splitters and combiners, separate straight waveguides, and a small number of long-path spiral waveguides to accurately assess the propagation loss on

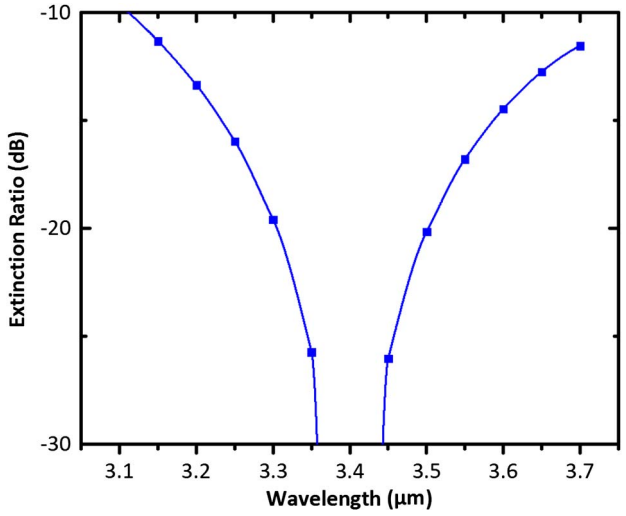

Fig. 3. Simulated optical bandwidth of the SiLN modulator for a center operation wavelength of 3.39 μm. Blue squares show discrete simulation points and the blue line is spline-fitted to these points.

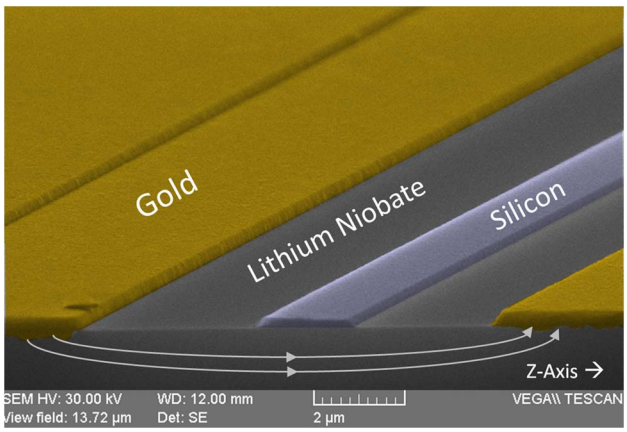

Fig. 4. Scanning electron micrograph of the cross-section of a SiLN modulator. The white lines crossing underneath the silicon represent the direction of the applied electric field during modulation.

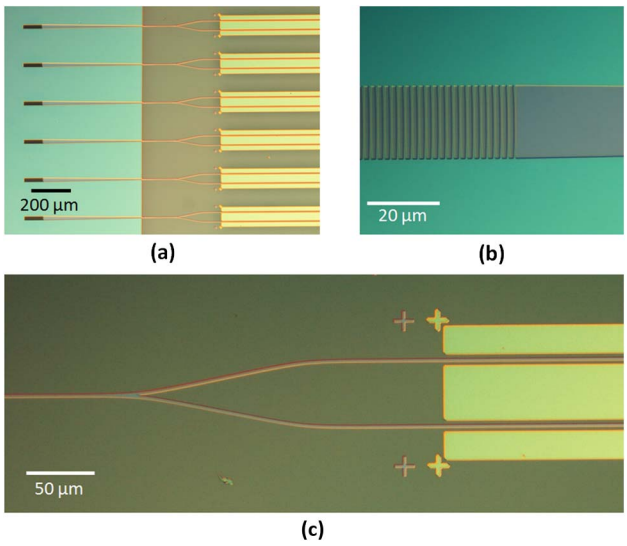

Fig. 5. Optical micrographs of a SiLN modulator chip: (a) wide view of chip showing half-etched (left) and full-etched (right) regions, (b) fiber-to-waveguide grating coupler, and (c) *Y* junction and modulator electrodes.

each sample. Light was coupled in and out of the fabricated chip via 20 µm wide, 1.7 µm period grating couplers followed by 630 µm long linear tapers to 2.1 µm wide, 210 nm thick waveguides. The active modulator section is 5 mm long.

The fabrication started with spin-coating the SiLN dies with ZEP-520A electron-beam resist. Electron-beam lithography was performed to open trenches in the resist. A 100 nm thick layer of SiO_2 was deposited into the trenches via electron-beam evaporation and liftoff, forming a hard mask for etching. The silicon was etched once with ICP-RIE by 110 nm, followed by masking of the grating couplers and an identical etch to form fully etched channel waveguides elsewhere on the chip. The SiO_2 hard-mask was then removed via dilute HF, and the die was subjected to low-temperature wet oxidation at 400°C for 1.5 hours to passivate the silicon surface with a ~3 nm thin oxide layer (this is discussed further in Section 3.A). Next, the metal electrodes with a gap of 8.5 µm were patterned via standard photolithography and liftoff of a 20 nm thin chromium adhesion layer followed by 216 nm of gold. Finally, the metal contacts were subjected to rapid thermal annealing at a temperature of 400°C for 30 s. A scanning electron micrograph of a finished sample is shown in Fig. 4, as well as optical micrographs of another sample in Fig. 5.

3. RESULTS AND DISCUSSION

A. Passive and Low-Frequency Characterization

The SiLN measurement setup is depicted in Fig. 6. A 2 mW continuous-wave helium–neon (HeNe) laser operating at 3.39 µm was used as the mid-IR source, coupled in through a fiber with an 18 µm core diameter at the input and coupled out through a large-area 400 µm core fiber to ease the alignment process. The output light was detected by a lead selenide (PbSe) detector with a specified bandwidth in the 10 kHz range. The light was chopped and then processed through a lock-in amplifier initially, but the chopper was removed once good fiber-to-grating coupler alignment was achieved.

First, the waveguide linear propagation loss was characterized. Straight waveguides 5.6 mm long were placed next to compact spiral waveguides which were 5.1 mm longer, using a bending radius of 300 µm. A propagation loss of 2.5 ± 0.7 dB/cm for the transverse electric mode is obtained by the cutback method after measuring two pairs of such waveguides. The loss figure presented is most likely not a consequence of etching-induced sidewall roughness, estimated here to be <50 nm rms, since the waveguides presented are relatively wide and measurements of earlier-produced half-etched SiLN waveguides yielded similar losses of 3–4 dB/cm. The loss may be due to contamination at the waveguide surface. The measurement wavelength of 3.39 µm exhibits strong optical absorption with hydrocarbons, which could affect the surface of the waveguide that is exposed to air during measurements. The 400°C wet oxidation step was crucial to reducing the propagation loss. Waveguides fabricated without this step exhibit propagation losses above 10 dB/cm. The mechanism of loss reduction is thought to be the passivation of dangling bonds at the silicon surface, reducing its adsorption of contaminants. Ultimately, the contamination-induced loss may be

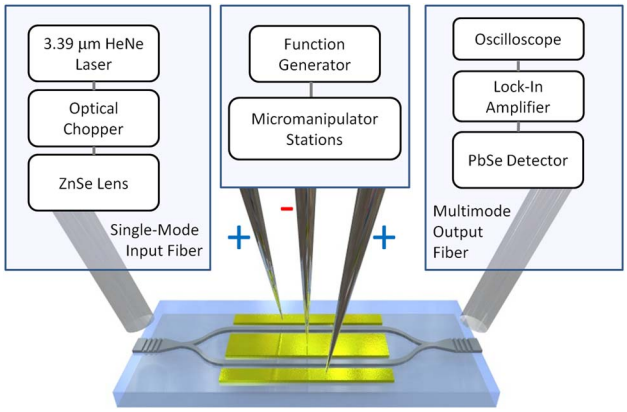

Fig. 6. Measurement setup used for characterization.

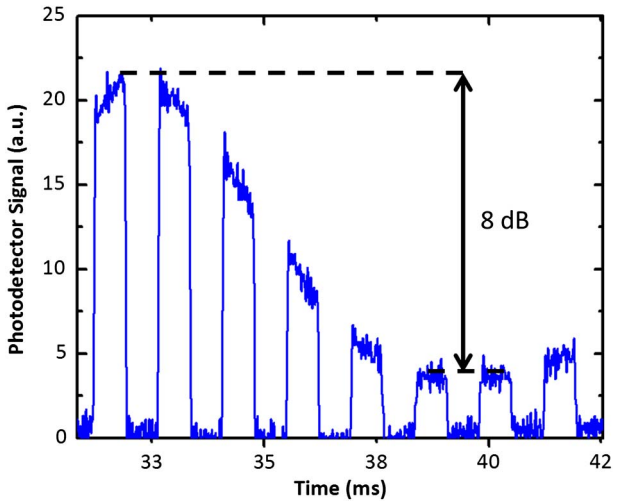

Fig. 7. Transmission through the device during simultaneous optical chopping at 700 Hz and optical modulation at 70 Hz. The photodetector signal (blue data line) has been shifted to emphasize the envelope.

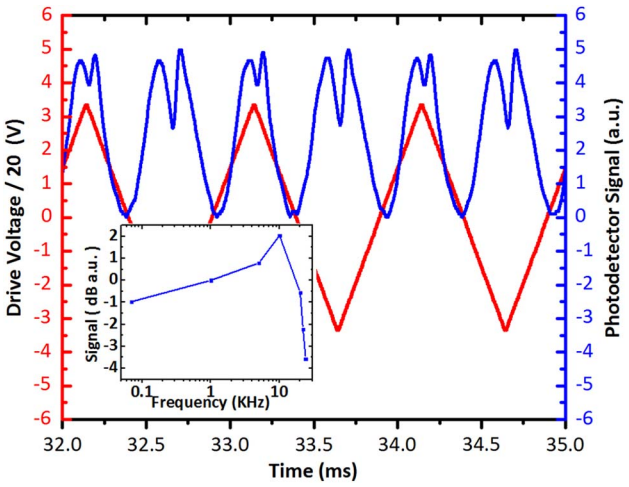

Fig. 8. SiLN modulator response. The red line is the modulator drive voltage divided by a factor of 20, and the blue line is the optical signal transmitted through the modulator, shifted for visibility. The inset shows the frequency response, limited by the detector speed.

mitigated with use of mid-IR compatible cladding materials such as chalcogenide glasses [32] deposited on the waveguide surface, or by hermetic packaging of the devices in an inert atmosphere.

Next, the modulators were characterized to determine the extinction ratio. The modulators were contacted with microprobes as shown in Fig. 6. A triangle-waveform voltage was applied to the modulator at 1/10 the frequency of the 700 Hz optical chopper used in the setup. Consequently, the square-wave chopper signal acquired a sinusoidal modulation envelope. By comparing the square-wave amplitude at the minimum and maximum of this envelope, we were able to obtain an AC characterization of the extinction ratio (Fig. 7). The chopper is necessary in this setup to obtain the relative values of maxima to minima. The measured extinction ratio is ~8 dB, which is lower than that predicted in Section 2.A. This can be attributed to an intensity mismatch between the two arms in the interferometer, probably resulting from small isolated interfacial bonding defects at the Si-$LiNbO_3$ interface. By using commercial vacuum wafer bonding systems, the density of these defects can be greatly reduced, resulting in higher-quality surfaces and better device performance.

The total on-chip insertion loss of the particular modulator under consideration was determined by comparing its unmodulated transmission to that of a straight waveguide of the same length. In addition to the modulator's propagation loss of 1.4 dB, an excess loss of 1.9 dB was observed. This can be attributed to several sources, such as point defects present in the lithography on that particular device, imperfections in the nanotip of the Y junction splitter, and increased metal electrode proximity resulting from an alignment error of 1 μm. Because of the close proximity of the standalone straight waveguides and the modulators, the coupling loss is nearly identical (verified by repeated measurements) and thus factored out. The on-chip insertion loss of the modulator is measured to be 3.3 ± 0.7 dB.

B. AC Modulation

The measurement of the half-wave voltage-length product, $V_\pi \cdot L$, was performed at 1 kHz (Fig. 8). The modulator was also measured out to the limit of the photodetector's bandwidth at 23 kHz (inset of Fig. 8), revealing an uneven frequency response of the detector at its limit. The slight distortion in the peaks of the signal is due to this behavior. The modulation speed measured in this experiment was limited by the speed of the detector available. With faster detectors and probes, and with travelling-wave electrode design, high-speed performance (>10 GHz bandwidth) mid-IR modulators are in principle feasible similar to conventional near-IR $LiNbO_3$ devices. Finally, to rule out the possibility of leakage effects and heating-induced phase changes, a multimeter was inserted into the voltage drive circuit, but no current flow was detected (sensitivity limit was 0.1 μA), indicating negligible power consumption at low frequencies.

The obtained $V_\pi \cdot L$ value from the modulation response is 26 V · cm, which is larger than the 13 V · cm value predicted in simulations. This difference is most likely not a result of dispersion in the r_{33} coefficient (which is negligible) [22]. One possible explanation could be the well-known phenomenon of domain realignment in $LiNbO_3$ after exposure to high-energy electron beams [33] such as the one used in pattern writing. Accordingly, the domains underneath the waveguide could be misaligned with respect to the polarization axis, causing a lowered effective electro-optic coefficient. Future studies with photolithography-patterned devices can investigate this possibility in order to resolve the discrepancy between measured and simulated values of $V_\pi \cdot L$.

4. CONCLUSION

In this work, we have demonstrated optical modulation in the mid-IR range on the proposed SiLN platform, utilizing the Pockels effect. A maximum modulation frequency of 23 kHz was observed (limited only by the detector speed), with an

extinction ratio of ~8 dB, an on-chip insertion loss of 3.3 dB, and a $V_\pi \cdot L$ of 26 V · cm, at a measurement wavelength of 3.39 μm. In addition, optical waveguides were characterized on the SiLN platform in the mid-IR, showing low TE-mode propagation losses of 2.5 dB/cm. With its compact waveguides, high electro-optic sensitivity, and strong second-order nonlinearities, this platform will enable high-performance photonic chips to be created for mid-IR applications.

FUNDING INFORMATION

National Science Foundation (NSF) CAREER (ECCS-1150672); Office of Naval Research (ONR) YIP (11296285).

ACKNOWLEDGMENT

The authors thank their colleagues, Ashutosh Rao and Marcin Malinowski, for helpful discussions in this work.

REFERENCES

1. R. Soref, "Mid-infrared photonics in silicon and germanium," Nat. Photonics **4**, 495–497 (2010).
2. B. Jalali and S. Fathpour, "Silicon photonics," J. Lightwave Technol. **24**, 4600–4615 (2006).
3. R. A. Soref, S. J. Emelett, and W. R. Buchwald, "Silicon waveguided components for the long-wave infrared region," J. Opt. A **8**, 840–848 (2006).
4. T. Baehr-Jones, A. Spott, R. Ilic, A. Spott, B. Penkov, W. Asher, and M. Hochberg, "Silicon-on-sapphire integrated waveguides for the mid-infrared," Opt. Express **18**, 12127–12135 (2010).
5. R. Shankar, I. Bulu, and M. Lončar, "Integrated high-quality factor silicon-on-sapphire ring resonators for the mid-infrared," Appl. Phys. Lett. **102**, 051108 (2013).
6. S. Khan, J. Chiles, J. Ma, and S. Fathpour, "Silicon-on-nitride waveguides for mid- and near-infrared integrated photonics," Appl. Phys. Lett. **102**, 121104 (2013).
7. J. Chiles, S. Khan, J. Ma, and S. Fathpour, "High-contrast, all-silicon waveguiding platform for ultra-broadband mid-infrared photonics," Appl. Phys. Lett. **103**, 151106 (2013).
8. H.-K. Hsiao, K. A. Winick, J. D. Monnier, and J.-P. Berger, "An infrared integrated optic astronomical beam combiner for stellar interferometry at 3-4 μm," Opt. Express **17**, 18489–18500 (2009).
9. B. Jalali, V. Raghunathan, R. Shori, S. Fathpour, D. Dimitropoulos, and O. Stafsudd, "Prospects for silicon mid-IR Raman lasers," IEEE J. Sel. Top. Quantum Electron. **12**, 1618–1627 (2006).
10. D. Borlaug, S. Fathpour, and B. Jalali, "Extreme value statistics in silicon photonics," IEEE Photon. J. **1**, 33–39 (2009).
11. R. K. W. Lau, M. R. E. Lamont, A. G. Griffith, Y. Okawachi, M. Lipson, and A. L. Gaeta, "Octave-spanning mid-infrared supercontinuum generation in silicon nanowaveguides," Opt. Lett. **39**, 4518–4521 (2014).
12. B. Kuyken, P. Verheyen, P. Tannouri, X. Liu, J. Van Campenhout, R. Baets, W. M. J. Green, and G. Roelkens, "Generation of 3.6 μm radiation and telecom-band amplification by four-wave mixing in a silicon waveguide with normal group velocity dispersion," Opt. Lett. **39**, 1349–1352 (2014).
13. A. Densmore, S. Janz, R. Ma, J. H. Schmid, D.-X. Xu, A. Delâge, J. Lapointe, M. Vachon, and P. Cheben, "Compact and low power thermo-optic switch using folded silicon waveguides," Opt. Express **17**, 10457 (2009).
14. M. Nedeljkovic, S. Stankovic, C. J. Mitchell, A. Z. Khokhar, S. A. Reynolds, D. J. Thomson, F. Y. Gardes, C. G. Littlejohns, G. T. Reed, and G. Z. Mashanovich, "Mid-infrared thermo-optic modulators in SoI," IEEE Photon. Technol. Lett. **26**, 1352–1355 (2014).
15. R. Soref and J. Larenzo, "All-silicon active and passive guided-wave components for λ = 1.3 and 1.6 μm," IEEE J. Quantum Electron. **22**, 873–879 (1986).
16. X. Tu, T.-Y. Liow, J. Song, X. Luo, Q. Fang, M. Yu, and G.-Q. Lo, "50-Gb/s silicon optical modulator with traveling-wave electrodes," Opt. Express **21**, 12776–12782 (2013).
17. D. J. Thomson, F. Y. Gardes, S. Liu, H. Porte, L. Zimmermann, J.-M. Fedeli, Y. Hu, M. Nedeljkovic, X. Yang, P. Petropoulos, and G. Z. Mashanovich, "High performance Mach–Zehnder-based silicon optical modulators," IEEE J. Sel. Top. Quantum Electron. **19**, 85–94 (2013).
18. M. Nedeljkovic, R. Soref, and G. Z. Mashanovich, "Free-carrier electrorefraction and electroabsorption modulation predictions for silicon over the 1–14-μm infrared wavelength range," IEEE Photon. J. **3**, 1171–1180 (2011).
19. B. Chmielak, M. Waldow, C. Matheisen, C. Ripperda, J. Bolten, T. Wahlbrink, M. Nagel, F. Merget, and H. Kurz, "Pockels effect based fully integrated, strained silicon electro-optic modulator," Opt. Express **19**, 17212–17219 (2011).
20. R. Palmer, S. Koeber, D. L. Elder, M. Woessner, W. Heni, D. Korn, M. Lauermann, W. Bogaerts, L. Dalton, W. Freude, J. Leuthold, and C. Koos, "High-speed, low drive-voltage silicon-organic hybrid modulator based on a binary-chromophore electro-optic material," J. Lightwave Technol. **32**, 2726–2734 (2014).
21. K. Noguchi, O. Mitomi, and H. Miyazawa, "Millimeter-wave Ti:$LiNbO_3$ optical modulators," J. Lightwave Technol. **16**, 615–619 (1998).
22. R. A. Becker, R. H. Rediker, and T. A. Lind, "Wide-bandwidth guided-wave electro-optic intensity modulator at λ = 3.39 μm," Appl. Phys. Lett. **46**, 809–811 (1985).
23. Y. S. Lee, G.-D. Kim, W.-J. Kim, S.-S. Lee, W.-G. Lee, and W. H. Steier, "Hybrid Si-$LiNbO_3$ microring electro-optically tunable resonators for active photonic devices," Opt. Lett. **36**, 1119–1121 (2011).
24. L. Chen, Q. Xu, M. G. Wood, and R. M. Reano, "Hybrid silicon and lithium niobate electro-optical ring modulator," Optica **1**, 112–118 (2014).
25. M. Solmaz and C. K. Madsen, "Silicon-on-lithium niobate waveguides for mid-infrared, " Proc. SPIE **6386**, 63860F (2006).
26. L. Cao, A. Aboketaf, Z. Wang, and S. Preble, "Hybrid amorphous silicon (a-Si:H)–$LiNbO_3$ electro-optic modulator," Opt. Commun. **330**, 40–44 (2014).
27. U. D. Dave, S. Uvin, B. Kuyken, S. Selvaraja, F. Leo, and G. Roelkens, "Telecom to mid-infrared spanning supercontinuum generation in hydrogenated amorphous silicon waveguides using a thulium doped fiber laser pump source," Opt. Express **21**, 32032–32039 (2013).
28. P. Rabiei, J. Ma, S. Khan, J. Chiles, and S. Fathpour, "Heterogeneous lithium niobate photonics on silicon substrates," Opt. Express **21**, 25573–25581 (2013).
29. J. Chiles and S. Fathpour, "Silicon on lithium niobate: A hybrid electro-optical platform for near- and mid-infrared photonics," in *Conference on Lasers and Electro-Optics*, OSA Technical Digest (online) (Optical Society of America, 2014), paper STh1M.6.
30. E. L. Wooten, K. M. Kissa, A. Yi-Yan, E. J. Murphy, D. A. Lafaw, P. F. Hallemeier, D. Maack, D. V. Attanasio, D. J. Fritz, G. J. McBrien, and D. E. Bossi, "A review of lithium niobate modulators for fiber-optic communications systems," IEEE J. Sel. Top. Quantum Electron. **6**, 69–82 (2000).
31. M. M. R. Howlader, T. Suga, and M. J. Kim, "Room temperature bonding of silicon and lithium niobate," Appl. Phys. Lett. **89**, 031914 (2006).
32. H. Lin, L. Li, Y. Zou, S. Danto, J. D. Musgraves, K. Richardson, S. Kozacik, M. Murakowski, D. Prather, P. T. Lin, V. Singh, A. Agarwal, L. C. Kimerling, and J. Hu, "Demonstration of high-Q mid-infrared chalcogenide glass-on-silicon resonators," Opt. Lett. **38**, 1470–1472 (2013).
33. H. Ito, C. Takyu, and H. Inaba, "Fabrication of periodic domain grating in $LiNbO_3$ by electron beam writing for application of nonlinear optical processes," Electron. Lett. **27**, 1221–1222 (1991).